Application of the Adiabatic Connection Random Phase Approximation to Electron-Nucleus Hyperfine Coupling Constants

Florian Bruder,[†] Florian Weigend,[†] and Yannick J. Franzke[*,‡]

†*Fachbereich Chemie, Philipps-Universität Marburg, Hans-Meerwein-Straße 4, 35032 Marburg, Germany*
‡*Otto Schott Institute of Materials Research, Friedrich Schiller University Jena, Löbdergraben 32, 07743 Jena, Germany*

E-mail: yannick.franzke@uni-jena.de

Abstract

The electron-nucleus hyperfine coupling constant is a challenging property for density functional methods. For accurate results, hybrid functionals with a large amount of exact exchange are often needed and there is no clear "one-for-all" functional, which describes the hyperfine coupling interaction for a large set of nuclei. To alleviate this unfavorable situation, we apply the adiabatic connection random phase approximation (RPA) in its post-Kohn–Sham fashion to this property as a first test. For simplicity, only the Fermi-contact and spin–dipole terms are calculated within the non-relativistic and the scalar-relativistic exact two-component framework. This requires to solve a single coupled-perturbed Kohn–Sham equation to evaluate the relaxed density matrix, which comes with a modest increase in computational demands. RPA performs remarkably well and substantially improves upon its Kohn–Sham (KS) starting point while also reducing the dependence on the KS reference. For main-group systems, RPA outperforms global, range-separated, and local hybrid functionals—at similar computational costs. For transition-metal compounds and lanthanide complexes, a similar performance as for hybrid functionals is observed. In contrast, related post-Hartree–Fock methods such as Møller–Plesset perturbation theory or CC2 perform worse than semilocal density functionals.

Introduction

Molecular systems with an open-shell configuration such as organic radicals, transition-metal catalysts, or lanthanide complexes play an important role in many fields of chemistry and materials science. These open-shell systems are routinely characterized with electron paramagnetic resonance (EPR) spectroscopy.[1–5] Here, the g-tensor and the electron-nucleus hyperfine coupling (HFC) tensor are among the decisive quantities to interpret the respective EPR spectra. The g-tensor describes the interaction of the electron spin with the external magnetic field, whereas the hyperfine coupling describes the interaction of the electron and nuclear magnetic moments. This hyperfine tensor is made up of the Fermi-contact (FC), spin–dipole (SD), and the paramagnetic spin–orbit (PSO) interaction. In a simple non-relativistic picture, the FC term is directly related to the spin-excess density at the origin of the nucleus and purely isotropic, whereas the SD term constitutes the anisotropy of the tensor.[6–10] Inclusion of scalar-relativistic effects essentially leads to modifications of the respective FC and SD operators but the spin-density in the vicinity of the nuclei is still the key quantity.[11–18] Overall, the Fermi-contact (FC) term is of great interest for single molecule magnets (SMMs) and their application as molecular qubits for quantum information technologies.[19] Very large HFCs may be obtained if the PSO interaction is small and the FC term is large.[20,21] This can lead to so-called "clock transitions" and an increase in phase memory time,[21] as such SMMs are less sensitive towards quantum decoherence.[22,23]

To support the interpretation of the EPR spectra or the *in silico* design of magnetic materials such as SMMs, quantum-chemical methods are of great importance. However, the accurate description of the electronic structure of open-shell systems is a complicated task. Various methods from complete or restricted active space self-consistent field (CASSCF/RASSCF) approaches to coupled-cluster methods and density functional theory are routinely applied to EPR properties, see, e.g., refs. 24–29. For large systems, the latter is the method of choice in terms of feasibility. Unfortunately, the choice of the density functional approximation (DFA) is a non-trivial task, as the performance of a given DFA may be highly dependent on the given molecule or nucleus.[9,30–36]

Over the past two decades, the adiabatic connection random phase approximation[37–39] (RPA) has emerged as a useful tool in quantum chemistry and materials science.[40–76] RPA methods can be employed in a post-Kohn–Sham framework based on converged Kohn–Sham orbitals[40–61] or in a self-consistent fashion to account for the density-driven error.[69–75] Analytical derivatives for chemical properties were formulated for both frameworks.[77–81] Alternatively, the RPA correlation energy can be used as a functional ingredient in the context of double hybrid functionals[82] or σ-functionals.[83–88] Especially the latter class of functionals has received recent interest.

Already the simplest approximation, i.e. direct RPA (dRPA), shows many attractive features.[60,61] Although, dRPA correlation energies show a dependence on the underlying KS reference they are otherwise free from empiricism. When using non-empirical KS functionals such as the generalized gradient approximation (GGA) PBE[89] or the meta-generalized gradient approximations (meta-GGAs) TPSS[90] and r^{2}SCAN[91,92] an accurate first-principles DFT method is obtained. Second, it achieves similar accuracy as hybrid functionals without the need to compute Hartree–Fock (HF) exchange in each self-consistent field (SCF) iteration. When RPA is applied in post-Kohn–Sham framework, the SCF procedure is solved with a semilocal DFA, and the RPA correlation energy and HF exchange energy are computed only once. Third, RPA is applicable to small-gap systems which is a distinctive feature over other post-KS or post-HF approaches.

So far, the performance of RPA was mainly assessed for energies and geometry properties.[61] Magnetic properties are comparably unexplored. Notable studies in this regard are the application of dRPA to nuclear magnetic resonance (NMR) shieldings and shifts,[81,87] as well as its application to finite magnetic fields.[57,93] Given the success of RPA in quantum chemistry, further studies on the performance of RPA for magnetic properties such as EPR pa-

rameters are clearly desirable.

In this work, we assess the accuracy of the direct random phase approximation as a post-Kohn–Sham method for the Fermi-contact and the spin–dipole hyperfine coupling terms. This is done in a non-relativistic and in the scalar-relativistic exact two-component [94–96] (X2C) framework. The results are intended to serve as a first test across the periodic table of elements and help to guide future research directions for accurate predictions of EPR properties.

Computational Methods

Theory

The FC and SD term can be evaluated as expectation values, i.e. the matrix representation of the operators is contracted with the density matrix in the atomic orbital (AO) basis. In a non-relativistic framework, these hyperfine coupling contributions in atomic units read [10,13]

$$A_N^{\mathrm{FC}} = \frac{4\pi}{3c^2}\frac{2}{n_\alpha - n_\beta} P_N \sum_{\mu\nu} D^S_{\mu\nu} \langle\mu|\delta(\vec{r}_N)|\nu\rangle \tag{1}$$

$$A^{\mathrm{SD}}_{N,uv} = \frac{1}{2c^2}\frac{2}{n_\alpha - n_\beta} P_N \sum_{\mu\nu} D^S_{\mu\nu} \langle\mu|\frac{3r_{N,u}\, r_{N,v} - \delta_{uv}\, r_N^2}{r_N^5}|\nu\rangle \tag{2}$$

where $\delta(\vec{r}_N)$ denotes the Dirac delta distribution, δ_{uv} the Kronecker delta, and $D^S_{\mu\nu}$ the AO spin excess density matrix element of the basis functions μ, ν. c is the speed of light and u, v are the Cartesian directions. n_α and n_β is the number of α and β electrons, respectively. $\vec{r}_N$ denotes the electron-nucleus position vector and r_N refers to the norm. $P_N = \beta_e g_e \beta_N g_N$ collects the electron and nuclear g-factors g_e and g_N, as well as Bohr's magneton β_e, and the nuclear magneton β_N. With standard Kohn–Sham methods, the one-particle density matrix is available from the eigenvectors

$$D^{\mathrm{KS}}_{\mu\nu\sigma} = \sum_j^{\mathrm{occ}} C_{\mu j\sigma} C_{\nu j\sigma} \tag{3}$$

where σ denotes the spin, μ, ν the AO basis functions, and i the Kohn–Sham eigenstates. Here, the coefficients $C_{\mu j}$ of the ground-state calculation are real, and only occupied (occ) orbitals are included in the summation. For post-Kohn–Sham methods, the KS density matrix $\mathbf{D}^{\mathrm{KS}}$ is changed due to electron correlation and orbital relaxation contributions. Thus, the RPA density matrix reads

$$\mathbf{D}^{\mathrm{RPA}} = \mathbf{D}^{\mathrm{KS}} + \mathbf{T}^{\mathrm{AO}} + \mathbf{Z}^{\mathrm{AO}} \tag{4}$$

Here, $\mathbf{T}^{\mathrm{AO}}$ is the unrelaxed one-particle AO density matrix due to RPA correlation and $\mathbf{Z}^{\mathrm{AO}}$ is the relaxation-only one-particle AO density matrix. [78] This relaxed density matrix is also needed for RPA geometry gradients [77–79] and we briefly review its calculation with the resolution of the identity (RI) approximation as previously [78] implemented in the TURBOMOLE program suite. [97–101]

The RI-RPA correlation energy is defined with an imaginary frequency integration according to [42]

$$E^{\mathrm{RI\text{-}RPA}} = \frac{1}{2}\int_{-\infty}^{\infty}\frac{\mathrm{d}\omega}{2\pi}\,\mathrm{tr}\left[\ln\left\{\mathbf{1}_{\mathrm{aux}} + \mathbf{Q}(\omega)\right\} + \mathbf{Q}(\omega)\right] \tag{5}$$

where all quantities are calculated in the RI auxiliary space (aux). The matrix $\mathbf{Q}$ is defined as

$$\mathbf{Q} = 2\mathbf{B}^{\mathrm{T}}\mathbf{G}\mathbf{B} \tag{6}$$

with the three-index matrix

$$B_{pq\sigma P} = \sum_{\mu\nu Q} C_{\mu p\sigma} C_{\nu q\sigma} (\mu\nu|Q)(Q|P)^{-1} \tag{7}$$

Here, p, q denote general KS molecular orbitals (MOs) and P, Q the RI auxiliary basis functions. We use Mulliken notation for the electron repulsion integrals. $\mathbf{B}$ is also known from other methods such as second-order Møller–Plesset perturbation theory [102] (MP2) or CC2. [103,104] The remaining matrix $\mathbf{G}$ in the MO space is given as

$$\mathbf{G} = \mathbf{\Delta}\left(\mathbf{\Delta}^2 + \omega^2\mathbf{1}\right)^{-1} \tag{8}$$

with the energy-dependent matrix

$$\Delta_{ia\sigma jb\sigma'} = \delta_{\sigma\sigma'}(\varepsilon_a - \varepsilon_i)\,\delta_{ij}\delta_{ab} \tag{9}$$

i, j refer to occupied KS orbitals, whereas a, b refer to virtual KS orbitals. ε are the KS energy eigenvalues.

The density correction $\mathbf{T}$ is evaluated in the MO space as

$$T_{ij\sigma} = \int_{-\infty}^{\infty}\frac{\mathrm{d}\omega}{2\pi}\sum_a\left(\mathbf{M}(\omega) - \omega^2\mathbf{\Delta}^{-1}\tilde{\mathbf{M}}(\omega)\mathbf{\Delta}^{-1}\right)_{ia\sigma ja\sigma} \tag{10}$$

$$T_{ab\sigma} = -\int_{-\infty}^{\infty}\frac{\mathrm{d}\omega}{2\pi}\sum_i\left(\mathbf{M}(\omega) - \omega^2\mathbf{\Delta}^{-1}\tilde{\mathbf{M}}(\omega)\mathbf{\Delta}^{-1}\right)_{ia\sigma ib\sigma} \tag{11}$$

$\tilde{\mathbf{M}}$ is a symmetric supermatrix defined as

$$\tilde{\mathbf{M}} = \mathbf{G}\mathbf{B}\tilde{\mathbf{Q}}\mathbf{B}^{\mathrm{T}}\mathbf{G} \tag{12}$$

$$\tilde{\mathbf{Q}} = \left[\mathbf{1}_{\mathrm{aux}} - \mathbf{Q}(\omega)\right]^{-1} - \mathbf{1}_{\mathrm{aux}} \tag{13}$$

Note that the occupied-virtual and virtual-occupied block is zero due to missing relaxation terms. The calculation of this unrelaxed density correction is the most time-consuming step of an RI-RPA gradient and HFC calculation, as it asymptotically scales with $\mathcal{O}(N^4 \log N)$. N measures the size of the system. It is also the most demanding part in terms of memory and disk storage. [78] For the RPA density matrix, $\mathbf{T}$ is transformed to the AO space.

Orbital relaxation effects are included by solving the coupled-perturbed Kohn–Sham (CPKS) equation

$$\left(\mathbf{\Delta} + \mathbf{H}^+_{\mathbf{ovov}}\right)\mathbf{Z}_{\mathbf{ov}} = -\frac{1}{2}\mathbf{R} \tag{14}$$

Therefore, the relaxed density matrix $\mathbf{Z}$ only contributes to the occupied-virtual (ov) and virtual-occupied MO tensor space. The required matrix $\mathbf{H}^+$ generally reads

$$H^+_{ia\sigma jb\sigma'} = 2\sum_{\mu\nu\kappa\lambda} C_{\mu i\sigma} C_{\nu a\sigma}\left[(\mu\nu|\kappa\lambda)^{\mathrm{RI}} + f^{\mathrm{XC}}_{\mu\nu\sigma\kappa\lambda\sigma'}\right] C_{\kappa j\sigma'} C_{\lambda b\sigma'} \tag{15}$$

$\mathbf{H}^+$ includes the two-electron Coulomb integral in the RI approximation [105–107] (RI-J) and the exchange-correlation (XC) kernel f^{XC} of the underlying KS reference in the adiabatic approximation. The CPKS right-hand side $\mathbf{R}$ is given as

$$R_{ia\sigma} = 2\varepsilon^{\mathrm{HF}}_{ia\sigma} + \gamma_{ia\sigma} - \gamma_{ai\sigma} + \left(\mathbf{H}^+\mathbf{T}\right)_{ia\sigma} \tag{16}$$

where $\boldsymbol{\varepsilon}^{\mathrm{HF}}$ is obtained by calculating the Fock matrix at the converged KS orbitals. Here, the occupied-virtual block of the Hartree–Fock (HF) matrix in the MO space is non-zero, as the KS orbitals are not generally eigenfunctions of the Fock operator. Fi-

nally, the matrix γ is defined as

$$\gamma_{ap\sigma} = 2\int_{-\infty}^{\infty}\frac{d\omega}{2\pi}\sum_{j}\left(\mathbf{GB\tilde{Q}B}^{T}\right)_{ja\sigma jp\sigma} \quad (17)$$

$$\gamma_{ip\sigma} = 2\int_{-\infty}^{\infty}\frac{d\omega}{2\pi}\sum_{b}\left(\mathbf{GB\tilde{Q}B}^{T}\right)_{ib\sigma pb\sigma} \quad (18)$$

and the right-hand side can be accumulated. Then, only **Z** is left to be determined iteratively. Here, the single CPKS equation in Eq. 14 is solved similarly to excited-state properties.[108] The solution vector **Z** is subsequently transformed to the AO space to construct the RPA density matrix. Compared to the preceding calculation of the unrelaxed density correction **T**, this step is computationally inexpensive. Overall, the calculation of the HFC and other properties with the RI-RPA method[78] is computationally less demanding than RI-MP2[102] and RI-CC2 calculations,[103,104] which scale as $\mathcal{O}(N^5)$.

For an existing RPA gradient implementation, only the HFC matrix needs to be interfaced into the RPA module. This holds for both the non-relativistic and the scalar-relativistic framework, as the latter only affects the HFC matrix.

Computational Settings

First, we consider the test sets 1 (small main-group compounds) and 2 (large main-group compounds) of the Bartlett group described in ref. 30. Structures are taken from the literature and the same basis sets as in the original benchmark study are applied to allow for a consistent comparison to the coupled-cluster theory with singles, doubles, and and perturbative triples CCSD(T). We omitted the Be compounds of test set 1 and Zn-porphycene of test set 2 in the present work, as this simplifies the basis set and auxiliary basis set settings. The aug-cc-pVTZ-J basis set,[109–111] taken from the Basis Set Exchange (BSE) library,[112–115] is employed for all elements. To cover the most important rungs of Jacob's ladder in DFT,[116,117] we apply the pure functionals BP86,[118,119] BLYP,[118,120] PBE,[89] TPSS,[90] and r^{2}SCAN[91,92] as well as the global hybrids PBE0,[121] TPSSh,[122] and r^{2}SCANh.[123] For PBE, the range-separated hybrid LC-ωPBE[124] and the local hybrid LH14t-calPBE[125] are further employed. The latter class is additionally represented by LH20t[126] and TMHF.[33] Libxc is applied for r^{2}SCAN and r^{2}SCANh.[127–129] All local hybrid functionals make use of a seminumerical integration scheme.[130,131] Note that BLYP, PBE, TPSS, PBE0, and TPSSh were already included in the original study of ref. 30. We only consider the semilocal functionals BP86,[118,119] BLYP,[118,120] PBE,[89] TPSS,[90] and r^{2}SCAN[91,92] as KS reference for the RPA calculations. Large integration grids are used (grid size 5a without pruning).[132–134] For comparison HF, MP2, and CC2 calculations are carried out. For MP2 and CC2, the scaled same-spin (SCS) and scaled opposite-spin (SOS) variants are also applied with the standard factors.[135,136] RPA,[42] MP2,[102] and CC2[103] make use of the RI approximation with the aug-cc-pV6Z-RIFIT auxiliary basis sets[101,137] taken from the BSE library.[112–115] The RI approximation is not applied for the SCF procedure, which is converged with tight thresholds of 10^{-8} Hartree for the energies and 10^{-7} for the root mean square of the density matrix change. For MP2 and CC2, the threshold for the norm of the residual vector in the solution of the Z vector equations is set to 10^{-6}. The imaginary frequency integration for RPA is carried out with the Gauss–Legendre method and 120 integration points. We note in passing that 80 points are already sufficient for converged hyperfine coupling constants. All HF, MP2, CC2, DFT, and RPA calculations herein are performed with TURBOMOLE[97–101] for maximum consistency. For the evaluation of diethylaminyl, we chose to evaluate H6, H7, H10, H11 as one data point due to the symmetry of the molecule instead of splitting them up into two as done in ref. 30. Throughout this work, we list the results in MHz.

Second, we apply the RPA approach to a subset (ScO, TiF_3, MnF, MnO_3, $Mn(CO)_5$, $Fe(CO)_5^+$) of the transition metal complexes described in ref. 36. The structures of these complexes are optimized with the def2-TZVP basis set[138] and the TPSS functional[90] using a large grid (grid size 5 with pruning).[132,133] Derivatives of quadrature weights are included in the calculations. The D4 dispersion correction[139] is applied for the calculations, as well as the RI-J approximation with the def2-TZVP auxiliary basis set.[140] Tight convergence thresholds of 10^{-8} Hartree are chosen for the energies. For the structure optimization, the default convergence criteria of 10^{-6} Hartree and 10^{-3} Hartree/bohr were chosen. The optimizations are done within the following point group symmetries. TiF_3 was optimized within D_{3h} symmetry, MnO_3 within C_{3v} symmetry, and $Mn(CO)_5$ as well as $Fe(CO)_5^+$ within C_{4v} symmetry. ScO and MnF were optimized without symmetry constraints. We note in passing that the experimental reference postulates D_{3h} symmetry for MnO_3.[141] However, this symmetry is not obtained with the TPSS functional, but with the PBE0 functional. The wavefunction obtained with PBE0 depicts strong spin-contamination with $\langle S^2\rangle = 0.97$, which is why we chose to use the TPSS result. The calculations of the HFC constants are done with the same parameters and the same methods as for the test sets 1 and 2 of the Bartlett group. Only the auxiliary basis for RPA, MP2, and CC2 is changed. The aug-cc-pV6Z-RIFIT auxiliary basis sets are only used for the light atoms and the aug-cc-pV5Z-RIFIT auxiliary basis sets[142] taken from the BSE library[112–115] are used for the metal atoms because there is no aug-cc-pV6Z-RIFIT basis set available for these elements. The symmetries of the molecules are not exploited for the HFC calculations.

Third, we apply the RPA approach to lanthanide single molecule magnets with large hyperfine coupling constants, namely $[La(OAr^*)_3]^-$, $[Lu(NR_2)_3]^-$, and $[Lu(OAr^*)_3]^-$ with OAr* = 2,6-Ad_2-4-t-Bu-C_6H_2O, Ad = adamantyl, t-Bu= tert-butyl, R = $SiMe_3$ with Me = methyl.[21] To account for relativistic effects, we use the spin-free exact two-component (X2C) Hamiltonian in the diagonal local approximation to the unitary decoupling transformation (DLU),[143–145] as spin–orbit effects were shown to be small for these compounds.[18,32,146,147] A finite nucleus model with a Gaussian charge distribution[148] is applied for the scalar potential and the vector potential.[149,150] The x2c-TZVPall-2c basis set is applied for the lanthanide atoms, while the x2c-SVPall-2c basis set is used otherwise.[151] We use large grids (grid size 4a without pruning) for the numerical integration.[132–134] The PBE,[89] TPSS,[90] r^{2}SCAN[91,92] PBE0,[121] TPSSh,[122] r^{2}SCANh,[123] LC-ωPBE,[124] and LH14t-calPBE[125] functionals are considered. The SCF procedure is converged with tight thresholds of 10^{-8} Hartree for the energies and 10^{-7} for the root mean square of the density matrix change. A canonical orthogonalization with a threshold of 10^{-4} is employed to accelerate the SCF convergence. Only for the PBE, TPSS, and r^{2}SCAN calculations of $[La(OAr^*)_3]^-$ without COSMO (see the following sentences), the canoncial orthogonalization is disabled as it hindered the SCF convergence. The conductor-like screening model[152,153] (COSMO) is applied with the parameters for tetrahydrofurane (permittivity of 7.52) and the default radii are applied (La = 2.2230, Lu = 2.2230, C= 2.0000, O = 1.7200, H = 1.3000, Si = 2.2000, N = 1.8300; all radii in Ångström). The RI-J approximation is only used for the RPA calculations with a tailored fitting basis set (see Supporting Information). Principal components of the HFC tensor are obtained from the symmetric form of the tensor. Computationally optimized structures are taken from the literature.[21] Currently, the RPA relaxed density is computed without COSMO.[78] We estimate the impact of this error by performing semilocal DFT and RPA calculations without COSMO throughout, see Supporting Information.

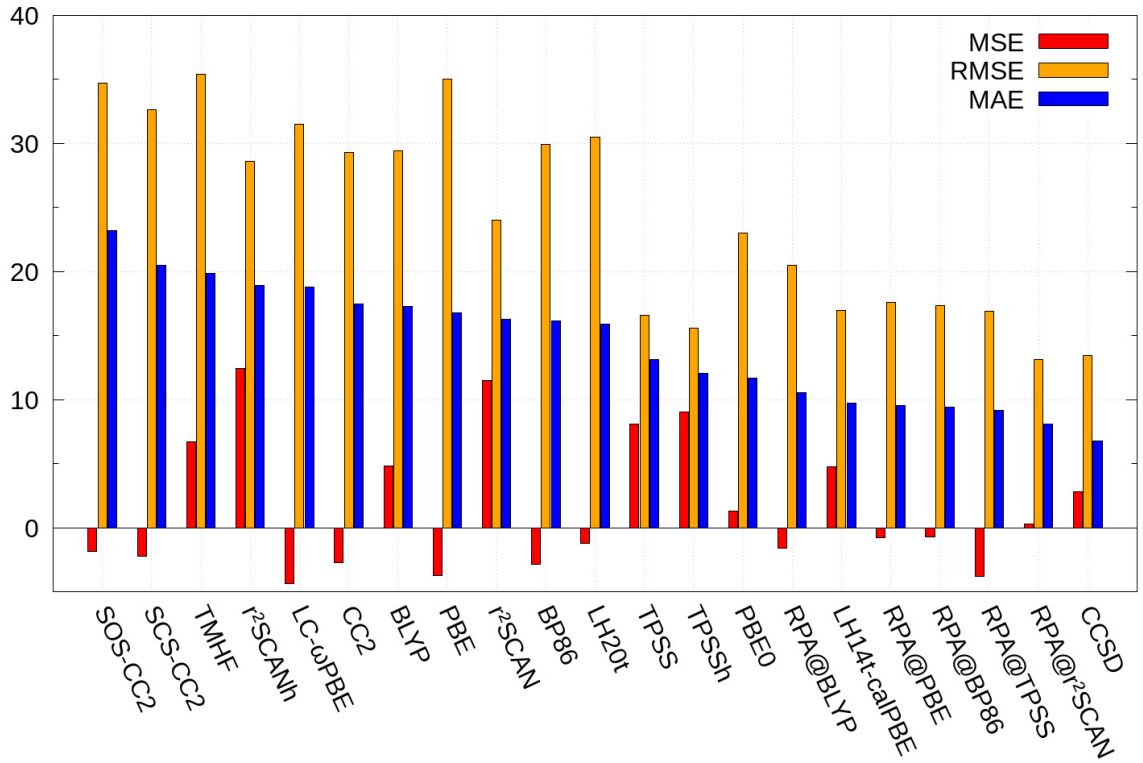

Figure 1: Statistical evaluation of various DFT methods for the test set 1 of ref. 30 consisting of 23 small main-group radials. Deviations are measured with respect to CCSD(T) results in MHz. Results with HF and MP2 are omitted in this figure, as large errors are observed with these methods. CCSD results are taken from ref. 30. Individual results and spin expectation values are listed in the Supporting Information. The set includes twenty-two ^{1}H, two ^{11}B, seventeen ^{13}C, four ^{14}N, eight ^{17}O, one ^{19}F, one ^{31}P, two ^{33}S, and one ^{35}Cl chemically inequivalent nuclei.

Results and Discussion

Small Main-Group Systems

A set of small main-group systems is considered first as high-level CCSD(T) results are available. It was shown that CCSD(T) performs excellently for the HFC of the given test set.[30] When neglecting spin–orbit effects and the PSO term, the isotropic HFC constant consists of the FC term, as the SD term only affects the anisotropy and the principal components. Thus, the comparison to CCSD(T) results essentially assesses the accuracy of the spin excess density at the respective nuclei. The mean signed errors (MSE), mean absolute errors (MAE), and root mean square errors (RMSE) for the test set composed out of the small main-group systems with respect to the CCSD(T) results for the HFC constants in ref. 30 are shown in Figure 1. RPA can be easily included in the accuracy ordering of ref. 30 right behind the coupled-cluster approaches. That is, the quality of the HFC constants for small organic radicals follow the ordering CCSD > RPA > Hybrid DFAs > Semilocal DFAs > CC2 > MP2 > HF. In contrast, a detailed ordering of the hybrid DFAs with global, range-separated, and local hybrids is difficult, as already observed in ref. 30 for GGA-based global hybrids, meta-GGA-based global hybrids, and range-separated hybrids. Removing nuclei with a HFC of more than 1000 MHz from the test set leads to essentially the same ordering, see Supporting Information.

Turning towards the DFT treatment in detail, the MAEs are clearly reduced and especially RPA performs excellently. Four of the five employed RPA approaches produce the four lowest MAEs. Only the local hybrid LH14t-calPBE leads to a lower MAE of 9.7 MHz in comparison to the "worst" RPA approach, namely RPA@BLYP. Additionally, the RPA MAEs are remarkably close together and span a range of 8.1 MHz (RPA@r^{2}SCAN) to 10.5 MHz (RPA@BLYP). In comparison, the MAEs for the corresponding pure functionals span a range from 13.1 MHz (TPSS) to 17.3 MHz (BLYP). However, this does not necessarily hold for all individual data points. Here, the GGA-based RPA results tend to be rather close to each other, while the meta-GGA-based results might deviate more. For instance, the HFC constants of CH are described very differently with RPA@TPSS compared to the other RPA approaches. The considered global hybrids span a range of 11.7 MHz (PBE0) to 18.9 MHz (r^{2}SCANh), whereas the PBE-based range-separated hybrid LC-ωPBE leads to an MAE of 18.8 MHz. The three local hybrids are very far apart with an MAE of 9.7 MHz for LH14t-calPBE, 15.9 MHz for LH20t and 19.9 MHz for TMHF. Therefore, RPA leads to the most notable improvement upon PBE and the admixture of exact exchange with global hybrids, range-separation, as well as a fully local admixture is inferior in this regard.

With respect to the RMSE, the RPA results are a somewhat more spread out and span a range of 13.2 MHz (RPA@r^{2}SCAN) to 20.5 MHz (RPA@BLYP). This makes RPA@r^{2}SCAN the best method in comparison to CCSD(T) for the small test set, as it produces both the lowest MAE and the lowest RMSE. For the other DFT approaches, the RMSE values are even more spread out. Functionals without exact exchange produce RMSEs from 16.6 MHz (TPSS) to 35.0 MHz (PBE), global hybrids from 15.7 MHz (TPSSh) to 23.0 MHz (PBE0), and local hybrids from 17.0 MHz (LH14t-calPBE) to 35.5 MHz (TMHF).

The excellent performance of RPA is even more remarkable when comparing it to MP2 and CC2 which come with increased

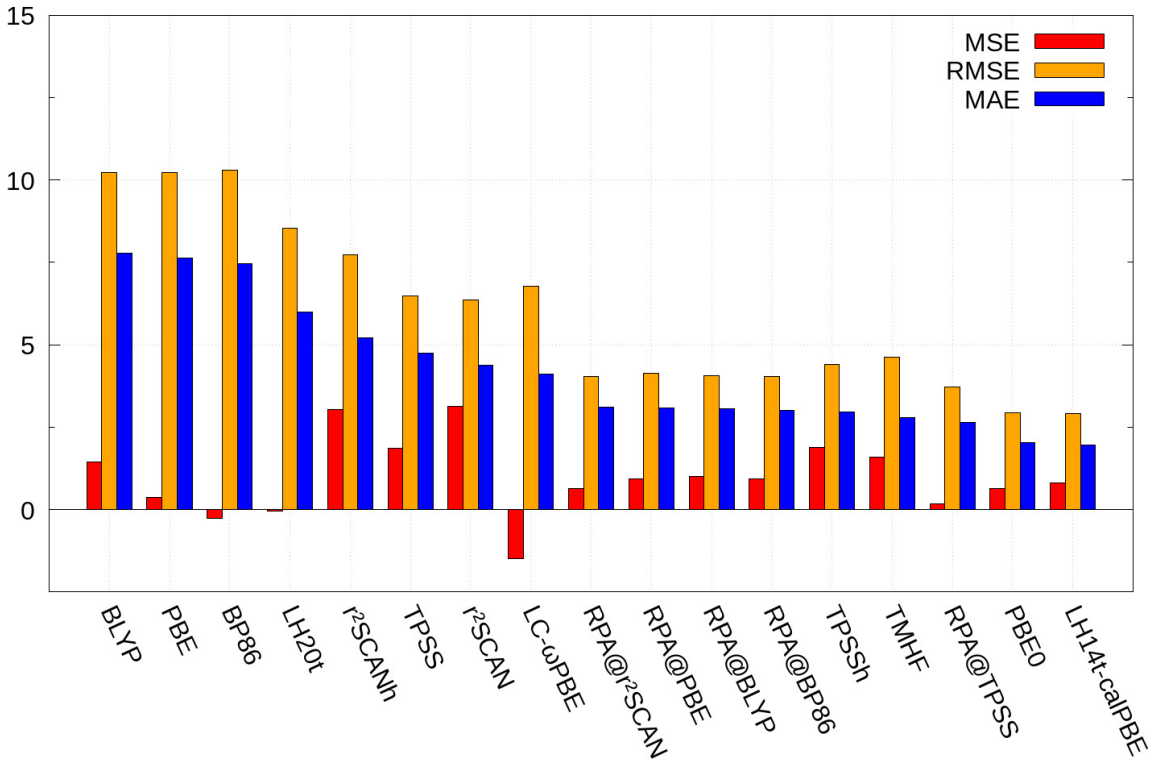

Figure 2: Statistical evaluation of various DFT methods for the test set 2 of ref. 30 consisting of 8 large main-group systems. Deviations are measured with respect to CCSD results in MHz. Results with HF, MP2, and CC2 are omitted in this figure, as large errors are observed with these methods. Individual results and spin expectation values are listed in the Supporting Information. The test set includes thirty-three ^{1}H, thirty-two ^{13}C, six ^{14}N, one ^{17}O, and one ^{33}S chemically inequivalent nuclei.

computational demands. HF and the MP2 methods lead to large MAE (ranging from 38.5 MHz for MP2 to 80.2 MHz for HF) and RMSE values (ranging from 57.9 MHz for MP2 to 111.3 MHz for HF). The different CC2 approaches lead to MAEs from 17.4 MHz (CC2) to 23.2 MHz (SOS-CC2) and to RMSEs from 29.3 MHz (CC2) to 34.7 MHz (SOS-CC2). Therefore, reliable post-HF results already require a very expensive treatment of electron correlation with at least CCSD.

We note that the performance of r^{2}SCAN observed in the present work is in striking contrast to the behavior found for its parent SCAN[154] in ref. 30. This can be rationalized by the pronounced grid sensitivity of SCAN,[91,155,156] which is especially detrimental for properties depending on the density in the vicinity of the nuclei. In line with our previous work on magnetic properties,[147,157–160] r^{2}SCAN is a rather stable and robust functional. Therefore, we recommend to only use r^{2}SCAN and not SCAN for EPR and RPA calculations.

Overall, the RPA approaches produces good results with respect to both the MAEs and the RMSEs. Especially RPA@r^{2}SCAN performs almost as good as CCSD. In comparison to established hybrid functionals, the results are of similar quality or even better. Additionally, the median RPA results are not notably reliant on the chosen DFA as starting point. All semilocal DFA starting points lead to very similar results, especially compared to the rather broad span of the results with semilocal DFT. Thus, RPA alleviates the difficult choice of finding the "right" DFA.

Large Main-Group Systems

The mean signed errors, mean absolute errors, and root mean square errors for the test set composed out of large organic systems with respect to the CCSD results for the HFC constants in ref. 30 are shown in Figure 2. Results for all employed methods are depicted, except for HF, MP2 and CC2 methods because of large MAEs, ranging from 17.6 MHz for CC2 to 44.1 MHz for HF. The same holds for the RMSE values, ranging from 24.8 MHz for CC2 to 58.2 MHz for HF. Note that the MAEs and RMSEs for this test set are generally smaller, which is at least partly caused by the overall smaller values of the calculated HFC constants.

For the MAEs, the RPA approach produces good but not the best results. Here, the MAEs range from 2.6 MHz (RPA@TPSS) to 3.1 MHz (RPA@r^{2}SCAN), which is again a remarkably small margin. For the individual data points, the RPA results based on the GGAs tend to be closer together and the results based on the meta-GGAs deviate slightly more from them. This shows again that the post-KS RPA still depends on the underlying KS density functional approximation and self-consistent RPA would be needed to remove this dependence. Of course, self-consistency comes with increased computational costs and the electron density of open-shell systems is often challenging to converge.

The PBE based local hybrid LH14t-calPBE features the lowest MAE with a value of 2.0 MHz, while LH20t gives the largest MAE of 6.0 MHz among the considered local hybrids. For both test sets, LH20t and TMHF are less robust than LH14t-calPBE. Global hybrids span a range from 2.0 MHz (PBE0) to 5.2 MHz (r^{2}SCANh) and the pure functionals result in MAEs from 4.4 MHz (r^{2}SCAN) to 7.8 MHz (BLYP). The range-separated LC-ωPBE leads to a mean error of 4.1 MHz. Just like for the first test set, the admixture of exact exchange worsens the performance of r^{2}SCAN, while application of the random phase approximation upon the semilocal DFA leads to an improvement.

The RMSE results are similar to the MAE results. For the RPA

Table 1: Isotropic hyperfine coupling constants (in MHz) of 3d transition metals within small compounds using various DFT methods and comparison to the experimental findings (Expt.) as collected in ref. 36. HF, MP2, and CC2 results are only given in the Supporting Information.

	ScO	TiF_3	MnF	MnO_3	$Mn(CO)_5$	$Fe(CO)_5^+$
BP86	1936	−220	492	1851	12	1
BLYP	2016	−224	520	1898	18	2
PBE	1872	−216	478	1844	10	0
TPSS	1762	−205	480	1792	15	2
r^2SCAN	1832	−223	522	1777	26	5
RPA@BP86	1663	−193	384	1682	5	−4
RPA@BLYP	1664	−192	384	1681	7	−4
RPA@PBE	1665	−193	384	1683	5	−4
RPA@TPSS	1694	−193	384	1687	9	−3
RPA@r^2SCAN	1684	−192	383	1669	6	−4
PBE0	1834	−184	434	1466	−1	−5
TPSSh	1758	−192	462	1669	10	−0
r^2SCANh	1841	−211	503	1646	22	3
LC-ωPBE	1863	−184	486	1649	31	1
LH14t-calPBE	1946	−192	464	1621	5	−4
LH20t	1899	−180	441	1547	2	−4
TMHF	1889	−195	504	1676	41	4
Expt.	1947	−185	442	1613	6	−2

approaches, the RMSEs appear in a close range from 3.7 MHz (RPA@TPSS) to 4.1 MHz (RPA@PBE). Results for the global hybrids range from 2.9 MHz (LH14t-calPBE) to 8.5 MHz (LH20t). For the local hybrids they range from 2.9 MHz (PBE0) to 7.7 MHz (r^2SCANh) and for the pure functionals they are in the region of 6.5 MHz (TPSS) to 10.3 MHz (BP86). LC-ωPBE leads to an RMSE of 6.8 MHz. Therefore, the ordering of accuracy according to RPA > Hybrid DFAs > Semilocal DFAs > CC2 > MP2 > HF is also valid for the test set with larger molecular systems.

To sum up the results of test sets 1 and 2, the RPA approaches produce very good MAE and RMSE values in comparison to the other considered methods. This holds for all tested starting points. Notably, also LH14t-calPBE, PBE0, and TPSSh produce very good results for both test sets. The robust performance of PBE0 and TPSSh was already observed in the original study of ref. 30. Concerning the range of the results for each rung of Jacob's ladder, RPA outperforms the semilocal and hybrid functionals. Additionally, RPA also clearly outperforms MP2 and CC2 representing post-Hartree–Fock methods—although these come with increased computational costs compared to RPA.

Transition-Metal Systems

In order to test whether the RPA approach can lead to good results for transition-metal systems, which are often studied with EPR experiments, a subset of the compounds investigated in ref. 36 is considered. To do so, small molecules with a known Fermi-contact HFC constant are studied. The electronic structure of ScO, TiF_3, MnO_3, $Mn(CO)_5$, and $Fe(CO)_5^+$ is made up of one unpaired electron, whereas that of MnF includes six unpaired electrons.

In Table 1, the calculated HFC constants of the 3d transition metals within those compounds are compared to experimental values,[141,161–165] which were collected in ref. 36. Only the results for the DFT based approaches are shown. HF, MP2, and CC2 results are listed in the Supporting information as these methods perform poorly. As expected, especially MP2 leads to very large errors.

As already observed for the first two test sets, the different RPA results are quite similar to each other and again relatively independent on the chosen DFA. The agreement with experiment is generally very good, with the exception of ScO. Here, the absolute deviations for the RPA approaches range from 253 MHz (RPA@TPSS) to 284 MHz (RPA@BP86) or from around 13% to 15%. This is larger than for any other of the considered methods, except for HF. The deviations of around 13% from the experimental value for MnF are also among the larger observed deviations for the considered DFT approaches. However, the RPA approaches work particularly well for the small HFC constants of $Mn(CO)_5$ and $Fe(CO)_5^+$. Here, the correct order of magnitude and the sign of the experiment is reproduced.

Additionally, the overall best results are obtained by LH14t-calPBE, which is in very good agreement for all of the considered experimental values. LH20t is also in very good agreement with experiment. Both give a correct description of the two small constants on $Mn(CO)_5$ and $Fe(CO)_5^+$. The other considered functionals give generally reasonable results with varying degrees of accuracy in terms of absolute values. A weak point is a good description of the small constants on $Mn(CO)_5$ and $Fe(CO)_5^+$. Often, one of the signs is wrong or the HFC constant on $Mn(CO)_5$ is too large in relative terms. Except for the RPA approaches, LH14t-calPBE, and LH20t, only TPSSh leads to good results for both small HFC constants.

Overall, RPA performs well for central atoms HFC of the considered transition-metal compounds. The results only clearly fall behind the very good agreement with experiment for LH14t-calPBE and LH20t. This is mainly due to larger deviations for ScO and MnF. The decisive point of the RPA approaches is again the relative independence of the results on the chosen DFA starting point. Additionally, the RPA approaches allow for a good description of two considered small HFCs. However, the set of considered molecules is relatively small and the PSO term needs to be generalized to RPA for broad applicability among transition-metal systems.

Lanthanide Single Molecule Magnets

In Table 2, calculated values for the principal components and the isotropic HFC constants of the three lanthanide single molecule magnets $[La(OAr^*)_3]^-$, $[Lu(NR_2)_3]^-$, and $[Lu(OAr^*)_3]^-$ are compared to the experimental findings of ref. 21. These molecules

Table 2: Principal components of the HFC-tensor A and the isotropic constant A_{iso} (in MHz) for the three spin-$\frac{1}{2}$ La(II) and Lu(II) molecules $[La(OAr^*)_3]^-$, $[Lu(NR_2)_3]^-$, and $[Lu(OAr^*)_3]^-$ with the scalar-relativistic DLU-X2C Hamiltonian and the x2c-TZVPall-2c/x2c-SVPall-2c basis set. Experimental results (Expt.) are taken from ref. 21. Isotropic constants and spin expectation values are listed in the Supporting Information. The experimental uncertainties for the principal components and the isotropic constants are ± 25 MHz for $[La(OAr^*)_3]^-$ and ± 50 for $[Lu(NR_2)_3]^-$ as well as $[Lu(OAr^*)_3]^-$.

	$[La(OAr^*)_3]^-$				$[Lu(NR_2)_3]^-$				$[Lu(OAr^*)_3]^-$			
Method	A_{11}	A_{22}	A_{33}	A_{iso}	A_{11}	A_{22}	A_{33}	A_{iso}	A_{11}	A_{22}	A_{33}	A_{iso}
PBE	1779	1779	1758	1772	2221	2221	2211	2218	3192	3192	3167	3184
TPSS	1764	1764	1729	1753	2266	2266	2240	2258	3189	3189	3145	3174
r^{2}SCAN	1810	1810	1733	1785	2386	2386	2328	2367	3269	3269	3189	3242
RPA@PBE	2033	2033	1981	2015	2450	2450	2413	2437	3388	3388	3331	3369
RPA@TPSS	2016	2016	1962	1998	2431	2431	2393	2418	3353	3353	3296	3334
RPA@r^{2}SCAN	2005	2005	1948	1986	2413	2413	2375	2400	3354	3354	3296	3335
PBE0	1845	1845	1788	1826	2268	2268	2234	2257	3278	3278	3217	3257
TPSSh	1789	1789	1741	1773	2275	2275	2241	2264	3216	3216	3161	3198
r^{2}SCANh	1847	1847	1760	1818	2394	2394	2330	2373	3304	3305	3215	3275
LC-ωPBE	2043	2043	1937	2008	2396	2396	2372	2388	3534	3535	3463	3510
LH14t-calPBE	1971	1971	1932	1958	2462	2462	2442	2455	3450	3450	3407	3436
Expt.	1870	1870	1780	1840	2480	2550	2300	2443	3500	3500	3400	3467

show very large hyperfine coupling constants and $[La(OAr^*)_3]^-$ and $[Lu(OAr^*)_3]^-$ consist of more than 200 atoms. Therefore, these complexes serve as an example for extended systems with a pronounced spin excess density at a heavy nucleus.

For the lanthanide systems, we broaden our view from the HFC constants to the principal components of the tensors, as these demonstrate the axial symmetry of the large molecules. Note that we only show scalar-relativistic results here. Due to the large s character of the unpaired electron,[21] the FC term dominates the HFC constant.[32] Therefore, a scalar-relativistic treatment is sufficient for the HFC constant, as shown in ref. 18. Matters are different for lanthanide systems with open f shells or more unpaired electrons.[16,25,32,147] Then, inclusion of spin–orbit coupling is key to accurate results.

Looking first at the principle components, the axial symmetry of the principle components is obtained with all methods. PBE severely underestimates the difference of A_{11} and A_{22} to A_{33}, whereas RPA@PBE and the hybrids alleviate this situation. As observed before, the RPA results span a smaller range than the pure DFA results they are based on. Especially, r^{2}SCAN deviates more notably from PBE and TPSS. Both RPA and the admixture of exact exchange leads to a very consistent increase of all principal components and consequently the isotropic hyperfine coupling constants. Therefore, RPA and hybrids clearly lead to an improvement for the Lu compounds, as semilocal DFAs such as PBE and TPSS substantially underestimate the hyperfine coupling. For the La complex, semilocal DFAs already lead to a very good agreement with the experiment. Here, RPA or range-separated and local hybrids result in too large hyperfine couplings.

The overall best result for the isotropic HFC constants of all three molecules is obtained for LH14t-calPBE with small deviations of 12 MHz and 54 MHz for $[Lu(NR_2)_3]^-$ and $[Lu(OAr^*)_3]^-$, respectively, and a very reasonable deviation of 118 MHz for $[La(OAr^*)_3]^-$. For the Lu complexes, the results of LH14t-calPBE are within the experimental uncertainties. The PBE-based functionals show that the hyperfine coupling is very sensitive towards the detailed admixture of exact exchange. RPA@PBE leads to results in the range of the three hybrids PBE0, LC-ωPBE, and LH14t-calPBE. Additionally, the RPA results of the different KS starting points are again very close together. The deviations are overall in the same region as for the other DFT approaches and the agreement with experiment is reasonable.

In terms of computational costs, the RPA calculations of the larger complexes $[La(OAr^*)_3]^-$ and $[Lu(OAr^*)_3]^-$ take roughly one day on a central processing unit of type Intel Xeon Gold 6212U at 2.40 GHz with 24 threads or about two days with 12 threads (shared memory parallelization with Open Multi-Processing). Overall, RPA in its post-KS fashion is easily applicable to extended systems when using the resolution of the identity approximation.[42,78]

To sum up, it is demonstrated that the RPA approach also works on large lanthanide systems with a spin excess density with pronounced s character. This was demonstrated both for the principle components of the HFC tensor and the isotropic HFC constant. In comparison to the other considered DFT methods, the RPA calculations do not result in the best agreement with experiment overall, but are generally on the same level as hybrid functionals. In a direct comparison between the RPA methods and the corresponding pure functionals for the HFC constants, the deviations for $[La(OAr^*)_3]^-$ were smaller with the respective KS reference, while the RPA results lead to a smaller deviation from experiment for $[Lu(NR_2)_3]^-$ and $[Lu(OAr^*)_3]^-$.

Conclusion

Our results show that RPA performs remarkably well for hyperfine coupling constants and tends to substantially improve upon its KS reference. It clearly outperforms post-Hartree–Fock methods such as MP2 and CC2, while coming with reduced computational demands. Notably, the RPA results only show a minor dependence on the KS reference. Moreover, RI-RPA is applicable to large molecules as shown for the lanthanide single molecule magnets with more than 200 atoms. This means that RPA is expected to become a useful tool for the study of EPR hyperfine coupling constants.

Extensions of the described framework are possible in multiple directions, namely the inclusion of the PSO term, extension to the class of σ-functionals, or the generalization to self-consistent RPA methods.

Supporting Information Available

Supporting Information is available with the structures optimized in this work and the Cartesian coordinates obtained from the Z-matrix information of ref. 30 (zip archive with txt files), employed RI-RPA auxiliary basis set for the lanthanide single molecule magnets (txt file), and complete data (zip archive with xlsx files).

Data Availability Statement

The data that support the findings of this study are available within the article and its supplementary material.

Author Contributions

Florian Bruder: Conceptualization (supporting); Data Curation (lead); Formal Analysis (lead); Investigation (lead); Methodology (equal); Software (supporting); Validation (equal); Writing - Original Draft (equal); Writing - Review & Editing (equal).
Florian Weigend: Conceptualization (supporting); Formal Analysis (supporting); Investigation (supporting); Methodology (equal); Supervision (lead); Visualization (supporting); Writing - Review & Editing (supporting).
Yannick J. Franzke: Conceptualization (lead); Data Curation (supporting); Formal Analysis (supporting); Investigation (supporting); Methodology (equal); Software (lead); Supervision (supporting); Validation (equal); Visualization (lead); Writing - Original Draft (equal); Writing - Review & Editing (equal).

Acknowledgement We thank Michael E. Harding (KIT) for supplying a preliminary RI auxiliary basis set for post-HF and post-KS methods to study the lanthanide single molecule magnets. F.B. and F.W. gratefully acknowledge support from the Deutsche Forschungsgemeinschaft (DFG, German Research Foundation) through the Collaborative Research Centre "4f for Future" (CRC 1573, project no. 471424360, project Q). Y.J.F. gratefully acknowledges support via the Walter–Benjamin programme funded by the Deutsche Forschungsgemeinschaft (DFG, German Research Foundation) — 518707327.

References

(1) Gerson, F.; Huber, W. *Electron Spin Resonance Spectroscopy of Organic Radicals*; Wiley-VCH: Weinheim, Germany, 2003.

(2) Kaupp, M., Bühl, M., Malkin, V. G., Eds. *Calculation of NMR and EPR Parameters: Theory and Applications*; Wiley-VCH: Weinheim, Germany, 2004.

(3) Neese, F. Quantum Chemistry and EPR Parameters. In *eMagRes*; Harris, R. K., Wasylishen, R. L., Eds.; John Wiley & Sons: Chichester, United Kingdom, 2017; Vol. 6; pp 1–22.

(4) Harriman, J. E. *Theoretical Foundations of Electron Spin Resonance*; Physical Chemistry: A Series of Monographs; Academic Press: New York, USA, 1978; Vol. 37.

(5) Goldfarb, D., Stoll, S., Eds. *EPR Spectroscopy: Fundamentals and Methods*; John Wiley & Sons: Chichester, United Kingdom, 2018.

(6) Perera, S. A.; Watts, J. D.; Bartlett, R. J. A theoretical study of hyperfine coupling constants. *J. Chem. Phys.* **1994**, *100*, 1425–1434.

(7) Perera, S. A.; Salemi, L. M.; Bartlett, R. J. Hyperfine coupling constants of organic radicals. *J. Chem. Phys.* **1997**, *106*, 4061–4066.

(8) Eriksson, L. A. ESR Hyperfine Calculations. In *Encyclopedia of Computational Chemistry*; Schleyer, P. v. R., Ed.; John Wiley & Sons: Chichester, United Kingdom, 1998.

(9) Simone Kossmann, B. K.; Neese, F. Performance of modern density functional theory for the prediction of hyperfine structure: meta-GGA and double hybrid functionals. *Mol. Phys.* **2007**, *105*, 2049–2071.

(10) Datta, D.; Gauss, J. Accurate Prediction of Hyperfine Coupling Tensors for Main Group Elements Using a Unitary Group Based Rigorously Spin-Adapted Coupled-Cluster Theory. *J. Chem. Theory Conput.* **2019**, *15*, 1572–1592.

(11) Malkin, E.; Malkin, I.; Malkina, O. L.; Malkin, V. G.; Kaupp, M. Scalar relativistic calculations of hyperfine coupling tensors using the Douglas–Kroll–Hess method with a finite-size nucleus model. *Phys. Chem. Chem. Phys.* **2006**, *8*, 4079–4085.

(12) Sandhoefer, B.; Kossmann, S.; Neese, F. Derivation and assessment of relativistic hyperfine-coupling tensors on the basis of orbital-optimized second-order Møller–Plesset perturbation theory and the second-order Douglas–Kroll–Hess transformation. *J. Chem. Phys.* **2013**, *138*, 104102.

(13) Autschbach, J.; Patchkovskii, S.; Pritchard, B. Calculation of Hyperfine Tensors and Paramagnetic NMR Shifts Using the Relativistic Zeroth-Order Regular Approximation and Density Functional Theory. *J. Chem. Theory Comput.* **2011**, *7*, 2175–2188.

(14) Autschbach, J. Perspective: Relativistic effects. *J. Chem. Phys.* **2012**, *136*, 150902.

(15) Autschbach, J. Relativistic Effects on Electron–Nucleus Hyperfine Coupling Studied with an Exact 2-Component (X2C) Hamiltonian. *J. Chem. Theory Comput.* **2017**, *13*, 710–718.

(16) Feng, R.; Duignan, T. J.; Autschbach, J. Electron–Nucleus Hyperfine Coupling Calculated from Restricted Active Space Wavefunctions and an Exact Two-Component Hamiltonian. *J. Chem. Theory Comput.* **2021**, *17*, 255–268.

(17) Gillhuber, S.; Franzke, Y. J.; Weigend, F. Paramagnetic NMR Shielding Tensors and Ring Currents: Efficient Implementation and Application to Heavy Element Compounds. *J. Phys. Chem. A* **2021**, *125*, 9707–9723.

(18) Bruder, F.; Franzke, Y. J.; Weigend, F. Paramagnetic NMR Shielding Tensors Based on Scalar Exact Two-Component and Spin–Orbit Perturbation Theory. *J. Phys. Chem. A* **2022**, *126*, 5050–5069.

(19) Zadrozny, J. M.; Niklas, J.; Poluektov, O. G.; Freedman, D. E. Millisecond Coherence Time in a Tunable Molecular Electronic Spin Qubit. *ACS. Cent. Sci.* **2015**, *1*, 488–492.

(20) MacDonald, M. R.; Bates, J. E.; Ziller, J. W.; Furche, F.; Evans, W. J. Completing the series of +2 ions for the lanthanide elements: synthesis of molecular complexes of Pr^{2+}, Gd^{2+}, Tb^{2+}, and Lu^{2+}. *J. Am. Chem. Soc.* **2013**, *135*, 9857–9868.

(21) Kundu, K.; White, J. R. K.; Moehring, S. A.; Yu, J. M.; Ziller, J. W.; Furche, F.; Evans, W. J.; Hill, S. A 9.2-GHz clock transition in a Lu(II) molecular spin qubit arising from a 3,467-MHz hyperfine interaction. *Nat. Chem.* **2022**, *14*, 392–397.

(22) Wolfowicz, G.; Tyryshkin, A. M.; George, R. E.; Riemann, H.; Abrosimov, N. V.; Becker, P.; Pohl, H.-J.; Thewalt, M. L. W.; Lyon, S. A.; Morton, J. L. Atomic clock transitions in silicon-based spin qubits. *Nat. Nanotechnol.* **2013**, *8*, 561–564.

(23) Shiddiq, M.; Komijani, D.; Duan, Y.; Gaita-Ariño; Coronado, E.; Hill, S. Enhancing coherence in molecular spin qubits via atomic clock transitions. *Nature* **2016**, *531*, 348–351.

(24) Lan, T. N.; Kurashige, Y.; Yanai, T. Toward Reliable Prediction of Hyperfine Coupling Constants Using Ab Initio Density Matrix Renormalization Group Method: Diatomic $^2\Sigma$ and Vinyl Radicals as Test Cases. *J. Chem. Theory Comput.* **2014**, *10*, 1953–1967.

(25) Wysocki, A. L.; Park, K. Nature of Hyperfine Interactions in $TbPc_2$ Single-Molecule Magnets: Multiconfigurational Ab Initio Study. *Inorg. Chem.* **2020**, *59*, 2771–2780.

(26) Sharkas, K.; Pritchard, B.; Autschbach, J. Effects from Spin–Orbit Coupling on Electro–Nucleus Hyperfine Coupling Calculated at the Restricted Active Space Level for Kramers Doublets. *J. Chem. Theory Comput.* **2015**, *11*, 538–549.

(27) Kossmann, S.; Neese, F. Correlated ab Initio Spin Densities for Larger Molecules: Orbital-Optimized Spin-Component-Scaled MP2 Method. *J. Phys. Chem. A* **2010**, *114*, 11768–11781.

(28) Saitow, M.; Neese, F. Accurate spin-densities based on the domain-based local pair-natural orbital coupled-cluster theory. *J. Chem. Phys.* **2018**, *149*, 034104.

(29) Hermosilla, L.; Calle, P.; García de la Vega, J. M.; Sieiro, C. Density Functional Theory Predictions of Isotropic Hyperfine Coupling Constants. *J. Phys. Chem. A* **2005**, *109*, 1114–1124.

(30) Windom, Z. W.; Perera, A.; Bartlett, R. J. Benchmarking isotropic hyperfine coupling constants using (QTP) DFT functionals and coupled cluster theory. *J. Chem. Phys.* **2022**, *156*, 094107.

(31) Gohr, S.; Hrobárik, P.; Repiský, M.; Komorovský, S.; Ruud, K.; Kaupp, M. Four-Component Relativistic Density Functional Theory Calculations of EPR g- and Hyperfine-Coupling Tensors Using Hybrid Functionals: Validation on Transition-Metal Complexes with Large Tensor Anisotropies and Higher-Order Spin–Orbit Effects. *J. Phys. Chem. A* **2015**, *119*, 12892–12905.

(32) Franzke, Y. J.; Yu, J. M. Hyperfine Coupling Constants in Local Exact Two-Component Theory. *J. Chem. Theory Comput.* **2022**, *18*, 323–343.

(33) Holzer, C.; Franzke, Y. J. A Local Hybrid Exchange Functional Approximation from First Principles. *J. Chem. Phys.* **2022**, *157*, 034108.

(34) Franzke, Y. J.; Bruder, F.; Gillhuber, S.; Holzer, C.; Weigend, F. Paramagnetic Nuclear Magnetic Resonance Shifts for Triplet Systems and Beyond with Modern Relativistic Density Functional Methods. *J. Phys. Chem. A* **2024**, *128*, 670–686.

(35) Verma, P.; Autschbach, J. Relativistic Density Functional Calculations of Hyperfine Coupling with Variational versus Perturbational Treatment of Spin–Orbit Coupling. *J. Chem. Theory Comput.* **2013**, *9*, 1932–1948.

(36) Pantazis, D. A. First-Principles Calculation of Transition Metal Hyperfine Coupling Constants with the Strongly Constrained and Appropriately Normed (SCAN) Density Functional and its Hybrid Variants. *Magnetochemistry* **2019**, *5*, 69.

(37) Bohm, D.; Pines, D. A Collective Description of Electron Interactions. I. Magnetic Interactions. *Phys. Rev.* **1951**, *82*, 625–634.

(38) Langreth, D.; Perdew, J. The exchange-correlation energy of a metallic surface. *Solid State Commun.* **1975**, *17*, 1425–1429.

(39) Langreth, D. C.; Perdew, J. P. Exchange-correlation energy of a metallic surface: Wave-vector analysis. *Phys. Rev. B* **1977**, *15*, 2884–2901.

(40) Furche, F. Molecular tests of the random phase approximation to the exchange-correlation energy functional. *Phys. Rev. B* **2001**, *64*, 195120.

(41) Furche, F. Developing the random phase approximation into a practical post-Kohn–Sham correlation model. *J. Chem. Phys.* **2008**, *129*, 114105.

(42) Eshuis, H.; Yarkony, J.; Furche, F. Fast computation of molecular random phase approximation correlation energies using resolution of the identity and imaginary frequency integration. *J. Chem. Phys.* **2010**, *132*, 234114.

(43) Eshuis, H.; Furche, F. A Parameter-Free Density Functional That Works for Noncovalent Interactions. *J. Phys. Chem. Lett.* **2011**, *2*, 983–989.

(44) Eshuis, H.; Bates, J. E.; Furche, F. Electron correlation methods based on the random phase approximation. *Theor. Chem. Acc.* **2012**, *131*, 1084.

(45) Scuseria, G. E.; Henderson, T. M.; Sorensen, D. C. The ground state correlation energy of the random phase approximation from a ring coupled cluster doubles approach. *J. Chem. Phys.* **2008**, *129*, 231101.

(46) Henderson, T. M.; Scuseria, G. E. The connection between self-interaction and static correlation: a random phase approximation perspective. *Mol. Phys.* **2010**, *108*, 2511–2517.

(47) Toulouse, J.; Zhu, W.; Ángyán, J. G.; Savin, A. Range-separated density-functional theory with the random-phase approximation: Detailed formalism and illustrative applications. *Phys. Rev. A* **2010**, *82*, 032502.

(48) Ángyán, J. G.; Liu, R.-F.; Toulouse, J.; Jansen, G. Correlation Energy Expressions from the Adiabatic-Connection Fluctuation–Dissipation Theorem Approach. *J. Chem. Theory Comput.* **2011**, *7*, 3116–3130.

(49) Klopper, W.; Teale, A. M.; Coriani, S.; Pedersen, T. B.; Helgaker, T. Spin flipping in ring-coupled-cluster-doubles theory. *Chem. Phys. Lett.* **2011**, *510*, 147–153.

(50) Kaltak, M.; Klimeš, J.; Kresse, G. Low Scaling Algorithms for the Random Phase Approximation: Imaginary Time and Laplace Transformations. *J. Chem. Theory Comput.* **2014**, *10*, 2498–2507.

(51) Kállay, M. Linear-scaling implementation of the direct random-phase approximation. *J. Chem. Phys.* **2015**, *142*, 204105.

(52) Mezei, P. D.; Csonka, G. I.; Ruzsinszky, A.; Kállay, M. Construction and Application of a New Dual-Hybrid Random Phase Approximation. *J. Chem. Theory Comput.* **2015**, *11*, 4615–4626.

(53) Graf, D.; Beuerle, M.; Schurkus, H. F.; Luenser, A.; Savasci, G.; Ochsenfeld, C. Accurate and Efficient Parallel Implementation of an Effective Linear-Scaling Direct Random Phase Approximation Method. *J. Chem. Theory Comput.* **2018**, *14*, 2505–2515.

(54) Grundei, M. M. J.; Burow, A. M. Random Phase Approximation for Periodic Systems Employing Direct Coulomb Lattice Summation. *J. Chem. Theory Comput.* **2017**, *13*, 1159–1175.

(55) Holzer, C.; Gui, X.; Harding, M. E.; Kresse, G.; Helgaker, T.; Klopper, W. Bethe–Salpeter correlation energies of atoms and molecules. *J. Chem. Phys.* **2018**, *149*, 144106.

(56) Kühn, M. Correlation Energies from the Two-Component Random Phase Approximation. *J. Chem. Theory Comput.* **2014**, *10*, 623–633.

(57) Practical Post-Kohn–Sham Methods for Time-Reversal Symmetry Breaking References. *J. Chem. Theory Comput.* **2023**, *19*, 3131–3145.

(58) Holzer, C.; Franzke, Y. J. Beyond Electrons: Correlation and Self-Energy in Multicomponent Density Functional Theory. *ChemPhysChem* **2024**, e202400120.

(59) Heßelmann, A.; Görling, A. Random-phase approximation correlation methods for molecules and solids. *Mol. Phys.* **2011**, *109*, 2473–2500.

(60) Ren, X.; Rinke, P.; Joas, C.; Scheffler, M. Random-phase approximation and its applications in computational chemistry and materials science. *J. Mater. Sci.* **2012**, *47*, 7447–7471.

(61) Chen, G. P.; Voora, V. K.; Agee, M. M.; Balasubramani, S. G.; Furche, F. Random-Phase Approximation Methods. *Annu. Rev. Phys. Chem.* **2017**, *68*, 421–445.

(62) Pernal, K. Correlation energy from random phase approximations: A reduced density matrices perspective. *Int. J. Quantum Chem.* **2018**, *118*, e25462.

(63) Grüneis, A.; Marsman, M.; Harl, J.; Schimka, L.; Kresse, G. Making the random phase approximation to electronic correlation accurate. *J. Chem. Phys.* **2009**, *131*, 154115.

(64) Paier, J.; Janesko, B. G.; Henderson, T. M.; Scuseria, G. E.; Grüneis, A.; Kresse, G. Hybrid functionals including random phase approximation correlation and second-order screened exchange. *J. Chem. Phys.* **2010**, *132*, 094103.

(65) Bates, J. E.; Furche, F. Communication: Random phase approximation renormalized many-body perturbation theory. *J. Chem. Phys.* **2013**, *139*, 171103.

(66) Chen, G. P.; Agee, M. M.; Furche, F. Performance and scope of perturbative corrections to random-phase approximation energies. *J. Chem. Theory Comput.* **2018**, *14*, 5701–5714.

(67) Förster, A. Assessment of the Second-Order Statically Screened Exchange Correction to the Random Phase Approximation for Correlation Energies. *J. Chem. Theory Comput.* **2022**, *18*, 5948–5965.

(68) Nguyen, B. D.; Chen, G. P.; Agee, M. M.; Burow, A. M.; Tang, M. P.; Furche, F. Divergence of Many-Body Perturbation Theory for Noncovalent Interactions of Large Molecules. *J. Chem. Theory Comput.* **2020**, *16*, 2258–2273.

(69) Voora, V. K.; Balasubramani, S. G.; Furche, F. Variational generalized Kohn-Sham approach combining the random-phase-approximation and Green's-function methods. *Phys. Rev. A* **2019**, *99*, 012518.

(70) Voora, V. K. Molecular Electron Affinities Using the Generalized Kohn–Sham Semicanonical Projected Random Phase Approximation. *J. Phys. Chem. Lett.* **2021**, *12*, 433–439.

(71) Samal, B.; Voora, V. K. Modeling Nonresonant X-ray Emission of Second- and Third-Period Elements without Core-Hole Reference States and Empirical Parameters. *J. Chem. Theory Comput.* **2022**, *18*, 7272–7285.

(72) Yu, J. M.; Nguyen, B. D.; Tsai, J.; Hernandez, D. J.; Furche, F. Selfconsistent random phase approximation methods. *J. Chem. Phys.* **2021**, *155*, 040902.

(73) Riemelmoser, S.; Kaltak, M.; Kresse, G. Optimized effective potentials from the random-phase approximation: Accuracy of the quasiparticle approximation. *J. Chem. Phys.* **2021**, *154*, 154103.

(74) Graf, D.; Ochsenfeld, C. A range-separated generalized Kohn–Sham method including a long-range nonlocal random phase approximation correlation potential. *J. Chem. Phys.* **2020**, *153*, 244118.

(75) Hellgren, M.; Caruso, F.; Rohr, D. R.; Ren, X.; Rubio, A.; Scheffler, M.; Rinke, P. Static correlation and electron localization in molecular dimers from the self-consistent RPA and *GW* approximation. *Phys. Rev. B* **2015**, *91*, 165110.

(76) Joshi, P.; Voora, V. K. Generalized perturbative singles corrections to the random phase approximation method: Impact on noncovalent interaction energies of closed- and open-shell dimers. *J. Chem. Phys.* **2024**, *160*, 044104.

(77) Rekkedal, J.; Coriani, S.; Iozzi, M. F.; Teale, A. M.; Helgaker, T.; Pedersen, T. B. Communication: Analytic gradients in the random-phase approximation. *J. Chem. Phys.* **2013**, *139*, 081101.

(78) Burow, A. M.; Bates, J. E.; Furche, F.; Eshuis, H. Analytical First-Order Molecular Properties and Forces within the Adiabatic Connection Random Phase Approximation. *J. Chem. Theory Comput.* **2014**, *10*, 180–194.

(79) Mussard, B.; Szalay, P. G.; Ángyán, J. G. Analytical Energy Gradients in Range-Separated Hybrid Density Functional Theory with Random Phase Approximation. *J. Chem. Theory Comput.* **2014**, *10*, 1968–1979.

(80) Balasubramani, S. G.; Voora, V. K.; Furche, F. Static polarizabilities within the generalized Kohn–Sham semicanonical projected random phase approximation (GKS-spRPA). *J. Chem. Phys.* **2022**, *157*, 164107.

(81) Drontschenko, V.; Bangerter, F. H.; Ochsenfeld, C. Analytical Second-Order Properties for the Random Phase Approximation: Nuclear Magnetic Resonance Shieldings. *J. Chem. Theory Comput.* **2023**, *19*, 7542–7554.

(82) Grimme, S.; Steinmetz, M. A computationally efficient double hybrid density functional based on the random phase approximation. *Phys. Chem. Chem. Phys.* **2016**, *18*, 20926–20937.

(83) Fauser, S.; Trushin, E.; Neiss, C.; Görling, A. Chemical accuracy with σ-functionals for the Kohn–Sham correlation energy optimized for different input orbitals and eigenvalues. *J. Chem. Phys.* **2021**, *155*, 134111.

(84) Trushin, E.; Thierbach, A.; Görling, A. Toward chemical accuracy at low computational cost: Density-functional theory with σ-functionals for the correlation energy. *J. Chem. Phys.* **2021**, *154*, 014104.

(85) Bokdam, M.; Lahnsteiner, J.; Ramberger, B.; Schäfer, T.; Kresse, G. Assessing Density Functionals Using Many Body Theory for Hybrid Perovskites. *Phys. Rev. Lett.* **2017**, *119*, 145501.

(86) Erhard, J.; Fauser, S.; Trushin, E.; Görling, A. Scaled σ-functionals for the Kohn–Sham correlation energy with scaling functions from the homogeneous electron gas. *J. Chem. Phys.* **2022**, *157*, 114105.

(87) Glasbrenner, M.; Graf, D.; Ochsenfeld, C. Benchmarking the Accuracy of the Direct Random Phase Approximation and σ-Functionals for NMR Shieldings. *J. Chem. Theory Comput.* **2022**, *18*, 192–205.

(88) Fauser, S.; Förster, A.; Redeker, L.; Neiss, C.; Erhard, J.; Trushin, E.; Görling, A. Basis Set Requirements of σ-Functionals for Gaussian- and Slater-Type Basis Functions and Comparison with Range-Separated Hybrid and Double Hybrid Functionals. *J. Chem. Theory Comput.* **2024**, *20*, 2404–2422.

(89) Perdew, J. P.; Burke, K.; Ernzerhof, M. Generalized Gradient Approximation Made Simple. *Phys. Rev. Lett.* **1996**, *77*, 3865–3868.

(90) Tao, J.; Perdew, J. P.; Staroverov, V. N.; Scuseria, G. E. Climbing the Density Functional Ladder: Nonempirical Meta–Generalized Gradient Approximation Designed for Molecules and Solids. *Phys. Rev. Lett.* **2003**, *91*, 146401.

(91) Furness, J. W.; Kaplan, A. D.; Ning, J.; Perdew, J. P.; Sun, J. Accurate and Numerically Efficient r^2SCAN Meta-Generalized Gradient Approximation. *J. Phys. Chem. Lett.* **2020**, *11*, 8208–8215.

(92) Furness, J. W.; Kaplan, A. D.; Ning, J.; Perdew, J. P.; Sun, J. Correction to "Accurate and Numerically Efficient r^2SCAN Meta-Generalized Gradient Approximation". *J. Phys. Chem. Lett.* **2020**, *11*, 9248–9248.

(93) Holzer, C.; Teale, A. M.; Hampe, F.; Stopkowicz, S.; Helgaker, T.; Klopper, W. GW quasiparticle energies of atoms in strong magnetic fields. *J. Chem. Phys.* **2019**, *150*, 214112.

(94) Dyall, K. G. Interfacing relativistic and nonrelativistic methods. I. Normalized elimination of the small component in the modified Dirac equation. *J. Chem. Phys.* **1997**, *106*, 9618–9626.

(95) Kutzelnigg, W.; Liu, W. Quasirelativistic theory equivalent to fully relativistic theory. *J. Chem. Phys.* **2005**, *123*, 241102.

(96) Iliaš, M.; Saue, T. An infinite-order two-component relativistic Hamiltonian by a simple one-step transformation. *J. Chem. Phys.* **2007**, *126*, 064102.

(97) Ahlrichs, R.; Bär, M.; Häser, M.; Horn, H.; Kölmel, C. Electronic structure calculations on workstation computers: The program system TURBOMOLE. *Chem. Phys. Lett.* **1989**, *162*, 165–169.

(98) Furche, F.; Ahlrichs, R.; Hättig, C.; Klopper, W.; Sierka, M.; Weigend, F. Turbomole. *Wiley Interdiscip. Rev.: Comput. Mol. Sci.* **2014**, *4*, 91–100.

(99) Balasubramani, S. G.; Chen, G. P.; Coriani, S.; Diedenhofen, M.; Frank, M. S.; Franzke, Y. J.; Furche, F.; Grotjahn, R.; Harding, M. E.; Hättig, C. et al. TURBOMOLE: Modular program suite for *ab initio* quantum-chemical and condensed-matter simulations. *J. Chem. Phys.* **2020**, *152*, 184107.

(100) Franzke, Y. J.; Holzer, C.; Andersen, J. H.; Begušić, T.; Bruder, F.; Coriani, S.; Della Sala, F.; Fabiano, E.; Fedotov, D. A.; Fürst, S. et al. TURBOMOLE: Today and Tomorrow. *J. Chem. Theory Comput.* **2023**, *19*, 6859–6890.

(101) TURBOMOLE GmbH 2024; Developers' version of TURBOMOLE V7.8.1, a development of University of Karlsruhe and Forschungszentrum Karlsruhe GmbH, 1989-2007, TURBOMOLE GmbH, since 2007; available from `https://www.turbomole.org` (retrieved May 14, 2024).

(102) Weigend, F.; Häser, M. RI-MP2: first derivatives and global consistency. *Theor. Chem. Acc.* **1997**, *97*, 331–340.

(103) Hättig, C.; Weigend, F. CC2 excitation energy calculations on large molecules using the resolution of the identity approximation. *J. Chem. Phys.* **2000**, *113*, 5154–5161.

(104) Hättig, C. Geometry optimizations with the coupled-cluster model CC2 using the resolution-of-the-identity approximation. *J. Chem. Phys.* **2003**, *118*, 7751–7761.

(105) Vahtras, O.; Almlöf, J.; Feyereisen, M. W. Integral Approximations for LCAO-SCF Calculations. *Chem. Phys. Lett.* **1993**, *213*, 514–518.

(106) Eichkorn, K.; Treutler, O.; Öhm, H.; Häser, M.; Ahlrichs, R. Auxiliary Basis Sets to Approximate Coulomb Potentials. *Chem. Phys. Lett.* **1995**, *242*, 283–290.

(107) Deglmann, P.; Furche, F.; Ahlrichs, R. An efficient implementation of second analytical derivatives for density functional methods. *Chem. Phys. Lett.* **2002**, *362*, 511–518.

(108) Furche, F.; Krull, B. T.; Nguyen, B. D.; Kwon, J. Accelerating molecular property calculations with nonorthonormal Krylov space methods. *J. Chem. Phys.* **2016**, *144*, 174105.

(109) Provasi, P. F.; Aucar, G. A.; Sauer, S. P. A. The effect of lone pairs and electronegativity on the indirect nuclear spin–spin coupling constants in CH_2X (X=CH_2, NH, O, S): Ab initio calculations using optimized contracted basis sets. *J. Chem. Phys.* **2001**, *115*, 1324–1334.

(110) Provasi, P. F.; Sauer, S. P. A. Optimized basis sets for the calculation of indirect nuclear spin–spin coupling constants involving the atoms B, Al, Si, P, and Cl. *J. Chem. Phys.* **2010**, *133*, 054308.

(111) Hedegård, E. D.; Kongsted, J.; Sauer, S. P. A. Optimized Basis Sets for Calculation of Electron Paramagnetic Resonance Hyperfine Coupling Constants: aug-cc-pVTZ-J for the 3d Atoms Sc-Zn. *J. Chem. Theory Comput.* **2011**, *7*, 4077–4087.

(112) Feller, D. The role of databases in support of computational chemistry calculations. *J. Comput. Chem.* **1996**, *17*, 1571–1586.

(113) Schuchardt, K. L.; Didier, B. T.; Elsethagen, T.; Sun, L.; Gurumoorthi, V.; Chase, J.; Li, J.; Windus, T. L. Basis Set Exchange: A Community Database for Computational Sciences. *J. Chem. Inf. Model.* **2007**, *47*, 1045–1052.

(114) Pritchard, B. P.; Altarawy, D.; Didier, B.; Gibson, T. D.; Windus, T. L. New Basis Set Exchange: An Open, Up-to-Date Resource for the Molecular Sciences Community. *J. Chem. Inf. Model.* **2019**, *59*, 4814–4820.

(115) Basis Set Exchange Library, `https://www.basissetexchange.org/` (retrieved Arpil 9, 2024).

(116) Perdew, J. P.; Schmidt, K. Jacob's ladder of density functional approximations for the exchange-correlation energy. *AIP Conf. Proc.* **2001**, *577*, 1–20.

(117) Mardirossian, N.; Head-Gordon, M. Thirty years of density functional theory in computational chemistry: an overview and extensive assessment of 200 density functionals. *Mol. Phys.* **2017**, *115*, 2315–2372.

(118) Becke, A. D. Density-functional exchange-energy approximation with correct asymptotic behavior. *Phys. Rev. A* **1988**, *38*, 3098–3100.

(119) Perdew, J. P. Density-functional approximation for the correlation energy of the inhomogeneous electron gas. *Phys. Rev. B* **1986**, *33*, 8822–8824.

(120) Lee, C.; Yang, W.; Parr, R. G. Development of the Colle-Salvetti correlation-energy formula into a functional of the electron density. *Phys. Rev. B* **1988**, *37*, 785–789.

(121) Adamo, C.; Barone, V. Toward reliable density functional methods without adjustable parameters: The PBE0 model. *J. Chem. Phys.* **1999**, *110*, 6158–6170.

(122) Staroverov, V. N.; Scuseria, G. E.; Tao, J.; Perdew, J. P. Comparative assessment of a new nonempirical density functional: Molecules and hydrogen-bonded complexes. *J. Chem. Phys.* **2003**, *119*, 12129–12137.

(123) Bursch, M.; Neugebauer, H.; Ehlert, S.; Grimme, S. Dispersion corrected r^2SCAN based global hybrid functionals: r^2SCANh, r^2SCAN0, and r^2SCAN50. *J. Chem. Phys.* **2022**, *156*, 134105.

(124) Vydrov, O. A.; Scuseria, G. E. Assessment of a long-range corrected hybrid functional. *J. Chem. Phys.* **2006**, *125*, 234109.

(125) Arbuznikov, A. V.; Kaupp, M. Towards improved local hybrid functionals by calibration of exchange-energy densities. *J. Chem. Phys.* **2014**, *141*, 204101.

(126) Haasler, M.; Maier, T. M.; Grotjahn, R.; Gückel, S.; Arbuznikov, A. V.; Kaupp, M. A Local Hybrid Functional with Wide Applicability and Good Balance between (De)Localization and Left–Right Correlation. *J. Chem. Theory Comput.* **2020**, *16*, 5645–5657.

(127) Marques, M. A. L.; Oliveira, M. J. T.; Burnus, T. Libxc: A library of exchange and correlation functionals for density functional theory. *Comput. Phys. Commun.* **2012**, *183*, 2272–2281.

(128) Lehtola, S.; Steigemann, C.; Oliveira, M. J. T.; Marques, M. A. L. Recent developments in libxc – A comprehensive library of functionals for density functional theory. *SoftwareX* **2018**, *7*, 1–5.

(129) Libxc. Version 6.2.2, available from `https://www.tddft.org/programs/libxc/` (retrieved July 26, 2023).

(130) Plessow, P.; Weigend, F. Seminumerical calculation of the Hartree–Fock exchange matrix: Application to two-component procedures and efficient evaluation of local hybrid density functionals. *J. Comput. Chem.* **2012**, *33*, 810–816.

(131) Holzer, C. An improved seminumerical Coulomb and exchange algorithm for properties and excited states in modern density functional theory. *J. Chem. Phys.* **2020**, *153*, 184115.

(132) Treutler, O.; Ahlrichs, R. Efficient molecular numerical integration schemes. *J. Chem. Phys.* **1995**, *102*, 346–354.

(133) Treutler, O. Entwicklung und Anwendung von Dichtefunktionalmethoden. Dissertation (Dr. rer. nat.), University of Karlsruhe (TH), Germany, 1995.

(134) Franzke, Y. J.; Treß, R.; Pazdera, T. M.; Weigend, F. Error-consistent segmented contracted all-electron relativistic basis sets of double- and triple-zeta quality for NMR shielding constants. *Phys. Chem. Chem. Phys.* **2019**, *21*, 16658–16664.

(135) Grimme, S. Improved second-order Møller–Plesset perturbation theory by separate scaling of parallel- and antiparallel-spin pair correlation energies. *J. Chem. Phys.* **2003**, *118*, 9095–9102.

(136) Jung, Y.; Lochan, R. C.; Dutoi, A. D.; Head-Gordon, M. Scaled opposite-spin second order Møller–Plesset correlation energy: An economical electronic structure method. *J. Chem. Phys.* **2004**, *121*, 9793–9802.

(137) Hättig, C. Optimization of auxiliary basis sets for RI-MP2 and RI-CC2 calculations: Core-valence and quintuple-zeta basis sets for H to Ar and QZVPP basis sets for Li to Kr. *Phys. Chem. Chem. Phys.* **2005**, *7*, 59–66.

(138) Weigend, F.; Ahlrichs, R. Balanced basis sets of split valence, triple zeta valence and quadruple zeta valence quality for H to Rn: Design and assessment of accuracy. *Phys. Chem. Chem. Phys.* **2005**, *7*, 3297–3305.

(139) Caldeweyher, E.; Bannwarth, C.; Grimme, S. Extension of the D3 dispersion coefficient model. *J. Chem. Phys.* **2017**, *147*, 034112.

(140) Weigend, F. Accurate Coulomb-fitting basis sets for H to Rn. *Phys. Chem. Chem. Phys.* **2006**, *8*, 1057–1065.

(141) Ferrante, R. F.; Wilkerson, J. L.; Graham, W. R. M.; Weltner Jr., W. ESR spectra of the MnO, MnO_2, MnO_3, and MnO_4 molecules at 4 °K. *J. Chem. Phys.* **1977**, *67*, 5904–5913.

(142) Bross, D. H.; Hill, J. G.; Werner, H.-J.; Peterson, K. A. Explicitly correlated composite thermochemistry of transition metal species. *J. Chem. Phys.* **2013**, *139*, 094302.

(143) Peng, D.; Reiher, M. Local relativistic exact decoupling. *J. Chem. Phys.* **2012**, *136*, 244108.

(144) Peng, D.; Middendorf, N.; Weigend, F.; Reiher, M. An efficient implementation of two-component relativistic exact-decoupling methods for large molecules. *J. Chem. Phys.* **2013**, *138*, 184105.

(145) Franzke, Y. J.; Middendorf, N.; Weigend, F. Efficient implementation of one- and two-component analytical energy gradients in exact two-component theory. *J. Chem. Phys.* **2018**, *148*, 104410.

(146) Franzke, Y. J.; Yu, J. M. Quasi-Relativistic Calculation of EPR *g* Tensors with Derivatives of the Decoupling Transformation, Gauge-Including Atomic Orbitals, and Magnetic Balance. *J. Chem. Theory Comput.* **2022**, *18*, 2246–2266.

(147) Holzer, C.; Franzke, Y. J.; Pausch, A. Current density functional framework for spin–orbit coupling. *J. Chem. Phys.* **2022**, *157*, 204102.

(148) Visscher, L.; Dyall, K. G. Dirac-Fock atomic electronic structure calculations using different nuclear charge distributions. *At. Data Nucl. Data Tables* **1997**, *67*, 207–224.

(149) Franzke, Y. J.; Weigend, F. NMR Shielding Tensors and Chemical Shifts in Scalar-Relativistic Local Exact Two-Component Theory. *J. Chem. Theory Comput.* **2019**, *15*, 1028–1043.

(150) Franzke, Y. J.; Mack, F.; Weigend, F. NMR Indirect Spin–Spin Coupling Constants in a Modern Quasirelativistic Density Functional Framework. *J. Chem. Theory Comput.* **2021**, *17*, 3974–3994.

(151) Pollak, P.; Weigend, F. Segmented Contracted Error-Consistent Basis Sets of Double- and Triple-ζ Valence Quality for One- and Two-Component Relativistic All-Electron Calculations. *J. Chem. Theory Comput.* **2017**, *13*, 3696–3705.

(152) Klamt, A.; Schüürmann, G. COSMO: a new approach to dielectric screening in solvents with explicit expressions for the screening energy and its gradient. *J. Chem. Soc., Perkin Trans. 2* **1993**, 799–805.

(153) Schäfer, A.; Klamt, A.; Sattel, D.; Lohrenz, J. C. W.; Eckert, F. COSMO Implementation in TURBOMOLE: Extension of an efficient quantum chemical code towards liquid systems. *Phys. Chem. Chem. Phys.* **2000**, *2*, 2187–2193.

(154) Sun, J.; Ruzsinszky, A.; Perdew, J. P. Strongly Constrained and Appropriately Normed Semilocal Density Functional. *Phys. Rev. Lett.* **2015**, *115*, 036402.

(155) Bartók, A. P.; Yates, J. R. Regularized SCAN functional. *J. Chem. Phys.* **2019**, *150*, 161101.

(156) Mejía-Rodríguez, D.; Trickey, S. B. Comment on "Regularized SCAN functional" [J. Chem. Phys. 150, 161101 (2019)]. *J. Chem. Phys.* **2019**, *151*, 207101.

(157) Franzke, Y. J.; Holzer, C. Impact of the current density on paramagnetic NMR properties. *J. Chem. Phys.* **2022**, *157*, 031102.

(158) Franzke, Y. J.; Holzer, C.; Mack, F. NMR Coupling Constants Based on the Bethe–Salpeter Equation in the *GW* Approximation. *J. Chem. Theory Comput.* **2022**, *18*, 1030–1045.

(159) Franzke, Y. J.; Holzer, C. Current density functional framework for spin–orbit coupling: Extension to periodic systems. *J. Chem. Phys.* **2024**, *160*, 184101.

(160) Bruder, F.; Franzke, Y. J.; Holzer, C.; Weigend, F. Zero-Field Splitting Parameters within Exact Two-Component Theory and Modern Density Functional Theory Using Seminumerical Integration. *J. Chem. Phys.* **2023**, *159*, 194117.

(161) Childs, W. J.; Steimle, T. C. A molecular-beam-optical and radio frequency-optical double-resonance study of the A $^2\Pi_r$–X $^2\Sigma^+$ band system of scandium monoxide. *J. Chem. Phys.* **1988**, *88*, 6168–6174.

(162) De Vore, T. C.; Weltner Jr., W. Titanium difluoride and titanium trifluoride molecules: electron spin resonance spectra in rare-gas matrices at 4 K. *J. Am. Chem. Soc.* **1977**, *99*, 4700–4703.

(163) DeVore, T. C.; Van Zee, R. J.; Weltner Jr., W. High spin molecules: ESR of MnF and MnF_2 at 4°K. *J. Chem. Phys.* **1978**, *68*, 3522–3527.

(164) Howard, J. A.; Morton, J. R.; Preston, K. F. The EPR spectrum of $Mn(CO)_5$. *Chem. Phys. Lett.* **1981**, *83*, 226–228.

(165) Lionel, T.; Morton, J. R.; Preston, K. F. The EPR spectrum of a single crystal of chromium hexacarbonyl doped with $Fe(CO)_5$. *J. Chem. Phys.* **1982**, *76*, 234–239.